# Compact size 3D magnetometer based on magnetoresistive sensors

Gabriel António Nunes Farinha
*Under supervision of Prof. Susana Freitas*
*Instituto de Engenharia de Sistemas e Computadores, Microsistemas e Nanotecnologias*
*Universidade Técnica de Lisboa, Lisbon, Portugal*

This thesis presents the optimization of magnetoresistive sensors working by tunnel effect, classified as state of the art in magnetic detection, with the advantage of been produced with small dimensions, aiming the development of a magnetometer.

Stacks were deposited to produce this type of sensors, with amorphous barriers of *AlOx*. Strategies as shape anisotropy were used to allow the linearization of the sensors, achieving for top pinned a TMR of 35%, and for bottom pinned configurations a TMR of $29\%$, with both free and pinned layers composed by *(CoFe)B*. The incorporation of *NiFe* on the free layer allowed to have sensors with 0.05 mT of coercivity and TMR of $29\%$. The detectivity values obtained were 120 $nT/\sqrt{Hz}$ at low frequencies and 20 $nT/\sqrt{Hz}$ at high frequencies, with a noise density characterized by an Hooge parameter of $4.86 \times 10^{-9}$ $\mu m^2$.

The final device is a magnetometer, which is capable of measuring magnetic fields in three spatial dimensions, with a sensitivity of 5.6 mV/mT in the range of -10 mT and +10 mT, composed by 4 single sensors assembled on Wheatstone bridge configuration for each dimension.

**Keywords:** Magnetic tunnel junctions, 3D magnetometer, shape anisotropy linearization, *AlOx* barrier, Wheatstone bridge.

## I. INTRODUCTION

Magnetic sensors are extremely important nowadays. They are widely used, being integrated in many devices, such as mobile phones, medical devices and navigation tools. This thesis explores further applications, aiming developing/characterizing magnetic sensors to be implemented in, for example, spatial aircrafts. A magnetometer capable of measuring magnetic fields in the 3 dimensions of space, working with magnetoresistive sensors based on tunnel effect, is the goal of this thesis.

Magnetic tunnel junctions (MTJs) were first reported at low temperatures by Julliere [1]. This device is, in the most basic model, composed by two ferromagnetic layers with a non-magnetic spacer between them. This spacer is an insulating layer, which force the electrons to tunnel between the two ferromagnets. One of the ferromagnetic layers will remain fixed for fields at which the other layer will rotate, being one the reference layer and the other the free layer. Tunneling Magnetoresistance (TMR) is the variation of resistance of the device with the rotation of the free layer under the influence of an external magnetic field.

Along this thesis, strategies as shape anisotropy will be used to linearize the magnetoresistance response of the sensors. This consists on reducing the width of the pillar that composes the sensor, increasing the contribution of the self-demagnetizing energy. Both top pinned configurations and bottom pinned will be optimized. As presented in figure 1, all sensors are composed by synthetic antiferromagnetic layer (SAF), allowing to fix the magnetization of the reference layer for larger fields.

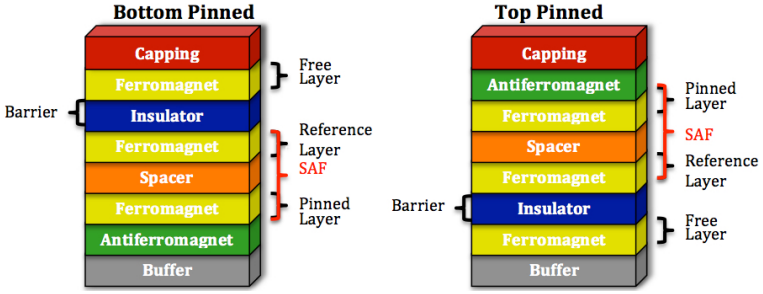


Figure 1: Magnetic tunnel junctions in both top pinned and bottomm pinned configuration. A SAF was used in the devices processed.

## II. EXPERIMENTAL WORK

MTJs were deposited using an industrial 6 inch wafer Ion Beam sputtering system (Nordiko 3000). The machine is composed by a load lock, a dealer and a deposition chamber, being ready to deposit up to eight 6 inch wafers per batch. The schematic of the machine's inside is presented in figure 2.

Different conditions can be used during deposition/etching. The table, where the substrate is attached by clamps, is allowed to rotate from 0-30 rpm, usually using a value of 15 rpm for depositions. The angle between the substrate and the horizontal can also be adjusted from 0 to 90 degrees. The RF coil is placed outside the chamber and the grids inside. The RF coil's supply a power signal of 13.56 MHz to the gas inside the chamber, generating a plasma. The three grids system accelerate the plasma and allows a uniform collimated ion beam. A shutter protects the substrate while the ion

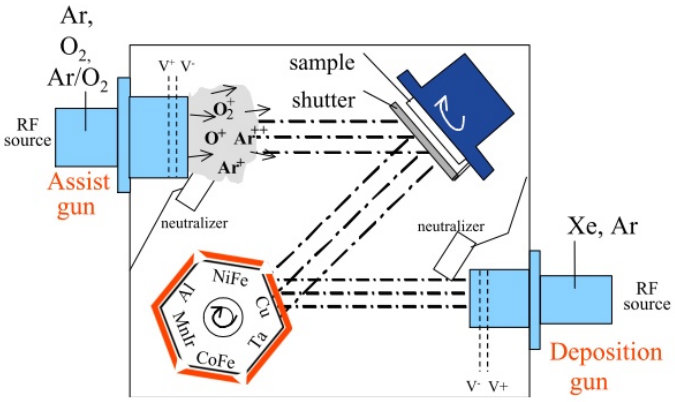


Figure 2: Schematic of Nordiko 3000 [2].

beam parameters are adjusted by the machine software. Once they are achieved, the shutter moves and an ion beam hits the target. The material sputtered from the target is then deposited into a nearby substrate to create a thin film. A permanent magnet creates a magnetic field of 4 mT near the substrate. To avoid surface charging, filamentless neutralizers are assembled beside each of the ion sources. The gun below is used for deposition, since the ion beam hits one of the six targets, allowing its particles to be ejected onto the substrate. The assist gun is usually used for etch or oxidation. The parameters used during depositions are presented in table I.

Table I: Deposition conditions used in Nordiko 3000. $V^+$ and $V^-$ are the potentials of each grid respectively.

| Beam Current | $V^+$ | $V^-$ | RF Power | Gas Flow | Table Angle |
|---|---|---|---|---|---|
| 24 mA | 1022 V | -300 V | 110 W | 2 sccm Xe | $80\,^\circ$ |

The machine has a base pressure of $3 \times 10^{-7}$ Torr, and a working pressure during a deposition process of $8 \times 10^{-5}$ Torr.

The deposition of a MTJ stack is composed by an intermediate step of oxidation. After depositing the barrier layer (*Al* in this case), it needs to be oxidized. This process occurs by the Remote Plasma method, that consists in creating a mixed Ar-$O_2$ plasma that is not accelerated by the grid, although the plasma itself creates a 12-14V potential difference between the grids. The $O_2$ ions reach the sample with their thermal energy. The RF source is applying power to the gas originating the plasma. The thickness of the barrier will depend of the previous thickness of Al deposited. The parameters used are presented in table II.

Table II: Parameters used on the barrier oxidation.

| Oxygen Flow | Argon Flow | Grids Voltage | RF Power |
|---|---|---|---|
| 40 sccm | 4 sccm | 0V | 110 W |

MTJs were fabricated with a conventional lithography/etch/liftoff process, figure 3. By first, a top electrode is defined by optical lithography, using a photoresist with $\approx 1.5\ \mu m$ of thickness. A dry etch, by ion beam sputtering on Nordiko 3600, is performed until the end of the substrate. The next lithography defines the rectangular pillars, with areas from 20 $\mu m^2$ up to 150 $\mu m^2$, protecting also the pads. A passivation layer is then deposited ($Al_2O_2$ with 1000 Å), allowing the isolation of the bottom electrode from the top electrode. The electrical contact between these two structures is achieved by liftoff, opening an access through the pillar's top. The last lithography defines the top electrode, followed by a deposition of $\approx 3000\ \mathring{A}$ of *AlSiCu*, with a passivation layer on top of *TiW(N)* with $\approx 150\ \mathring{A}$.

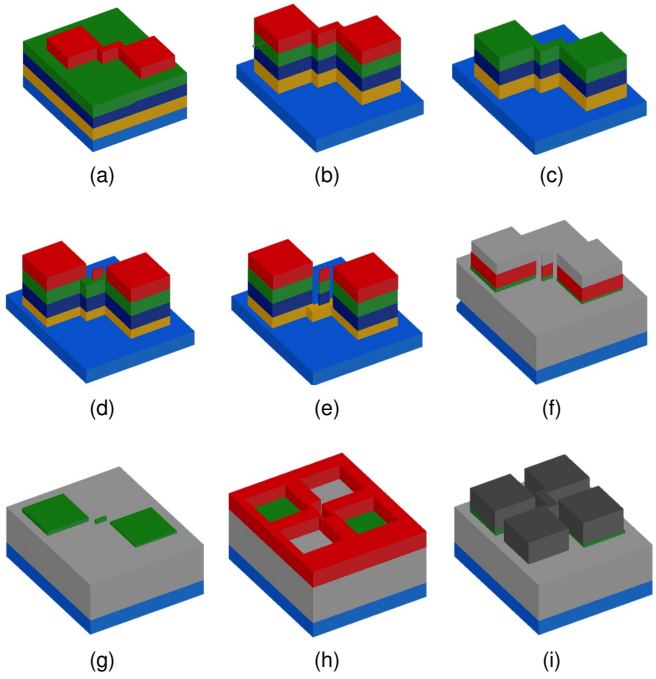


Figure 3: Schematic of the microfabrication process. (a) Bottom electrode definition by optical lithography. (b) Dry etch down to the substrate. (c) Resist Strip. (d) Junction definition by optical lithography. (e) Dry etch down to the buffer. (f) Oxide deposition. (g) Oxide lift off by ultrasounds in a solvent. (h) Top electrode definition by optical lithography. (i) Metal liftoff and final device.

Once the sensors are processed, they are assembled in bridge configuration. In this work, a full bridge configuration is used, with four MTJs playing the role of variable resistors, as presented in figure 4. Once the bridge has a differential output, given by $V = I\Delta R$ for a current (I) biased bridge, with $\Delta R$ being the difference between two sensors oriented in opposition directions and *V* the output, the noise from common sources is suppressed and its output is an offset-free signal. In the absence of an applied field, the bridge has a null output, since all the MTJs have the same resistance. Furthermore, this configuration provides a linear output and the one

with larger variation, when compared with other bridge configurations. The bridges mounted during this work are composed by four individual sensors, that were processed in the same sample, but diced before being assembled on a PCB, since they need to have different orientations for the pinned layer.

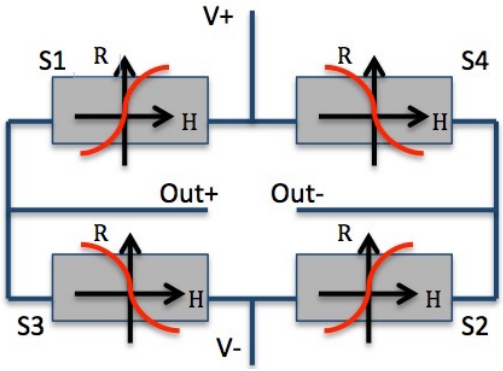


Figure 4: Full Wheatstone bridge configuration with 4 MTJ sensors.

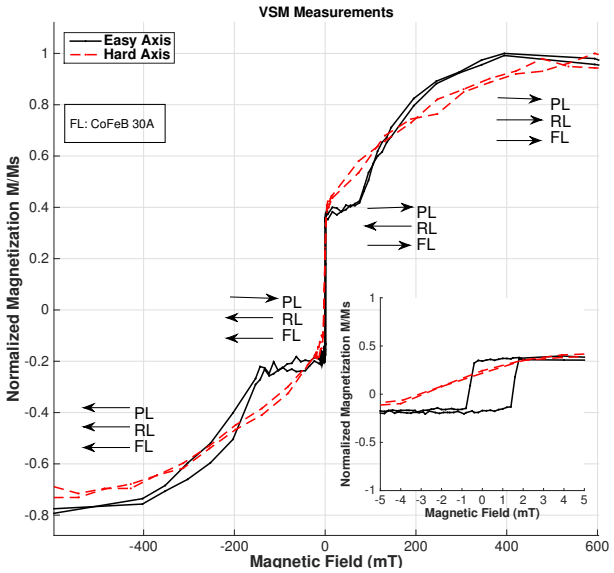


Figure 5: VSM curve for a bottom-pinned sample with SAF and a 30Å thick free layer.

## III. RESULTS

The final goal of this thesis is to have a magnetometer working with linear sensors and good TMR response, having a good detectivity and a low noise level if possible. To achieve this requirements, it was necessary to continue a process of optimization already started by the PhD Simon Knudde at INESC-MN. The results presented correspond to the optimization process realized with both bottom pinned and top pinned magnetic tunnel junction of alumina (*AlOx*), an amorphous barrier.

### A. Bottom pinned optimization

The first deposited samples with a bottom pined stack had a free layer of 30 Å. To check the magnetic stability of the deposited stack, measurements on VSM were perfomed, after an annealing treatment of 30 minutes at 250 $^{\circ}$C and cooling down inside 1 Tesla permanent magnet. The correspondent stack is composed by: Ru 150 Å/ CoFeB 30 Å/AlOx 9 Å/CoFeB 30 Å/Ru 9 Å/CoFe 22 Å/IrMn 180 Å/Ru 200 Å/Mg 4 Å/Ru 200 Å.

From the VSM results, it is possible to see the magnetic coupling between the different magnetic layers composing the stack. The pinned layer of the SAF has an exchange bias onto the anti-ferromagnet, leading to a stable plateau up to 140 mT. The exchange related with the RKKY coupling through the *Ru* spacer is about 76 mT.

The linearization strategy used was shape anisotropy, more precisely parallel anisotropy, with the easy axis of the pinned layer pointing to the same direction of the free layer. After patterning the sensors with rectangular shapes, the magnetization of the free layer will align itself along larger dimension of the pillar, staying perpendicular to the magnetization of the pinned layer at zero magnetic field.

The starting point of the optimization process consisted in changing the thickness and time of oxidation of the barrier. The first three samples (RP24, RP25, RP26) correspond to a thickness of aluminum of 7 Å, with times of oxidation of 10, 20 and 30 seconds respectively. The remaining samples (RP28, RP29, RP30) correspond to a thickness of aluminum of 9 Å, with times of oxidation of 20, 30 and 40 seconds respectively.

The resume of the results achieved is presented in table III, and the magnetic response is illustrated in figure 6.

From this first set of samples, it was possible to achieve some conclusions. There was good coupling between the magnetic layers, although a square response was obtained. The time of oxidation corresponding to the two different thickness could also be optimized, avoiding situations of under etch, sample RP24, or over etch, sample RP26, since the maximum value of TMR is expected to correspond to a situation of complete oxidation of the barrier, without damaging the layers nearby. The next steps consisted in: optimization of the free layer thickness, test of different barriers with a two-step deposition method, leading to linear sensors and an increase on the RA product. The final result of the optimization process is presented next. The corresponding stack is composed by: Ru 150 Å/ CoFeB **X**

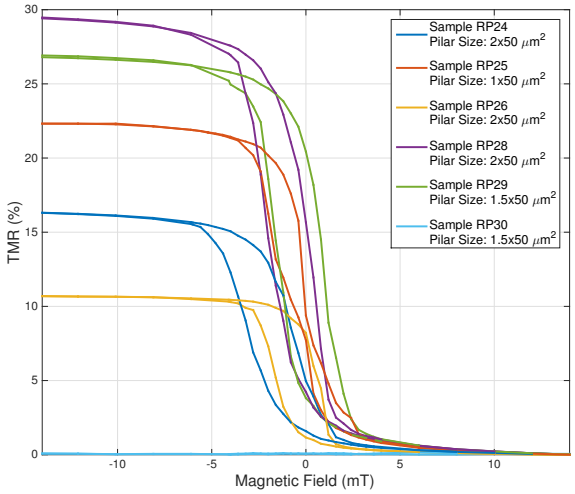


Figure 6: First set of bottom pinned samples. Square responses were obtained.

Table III: Resume of the results obtained for barrier optimization. Values corresponding to one pillar per sample.

| Sample ID | TMR (%) | R×A ($k\Omega.\mu m^2$) | $H_c$ (mT) | $H_f$ mT |
|---|---|---|---|---|
| RP24 | 16.32 | 0.09 | 1.16 | 1.87 |
| RP25 | 22.32 | 0.21 | 0.44 | 0.55 |
| RP26 | 10.70 | 0.41 | 1.09 | 0.53 |
| RP28 | 29.48 | 0.66 | 1.05 | 0.95 |
| RP29 | 26.92 | 1.91 | 1.18 | 0.30 |
| RP30 | 0.15 | - | - | - |

Å/AlOx 2×(7 Å + 15 seconds of oxidation) Å/CoFeB 40 Å/Ru 6 Å/CoFe 30 Å/IrMn 180 Å/Ru 400 Å, with **X** the thickness of the free layer presented in the graph of figure 7. The parameters characterizing each sensor are also presented in table IV.

Table IV: Resume of the results obtained for barrier optimization of figure 7.

| Sample | TMR (%) | $H_c$ (mT) | $H_f$ (mT) | R×A ($k\Omega.\mu m^2$) |
|---|---|---|---|---|
| RP82 | 18.72 | 0.58 | 0.34 | 93.85 |
| RP83 | 23.50 | 0.17 | 0.96 | 190.50 |
| RP84 | 21.74 | 0.28 | 0.99 | 84.10 |
| RP85 | 5.67 | 0.23 | 0.19 | 9.60 |
| RP86 | 21.16 | 0.23 | 1.15 | 78.75 |

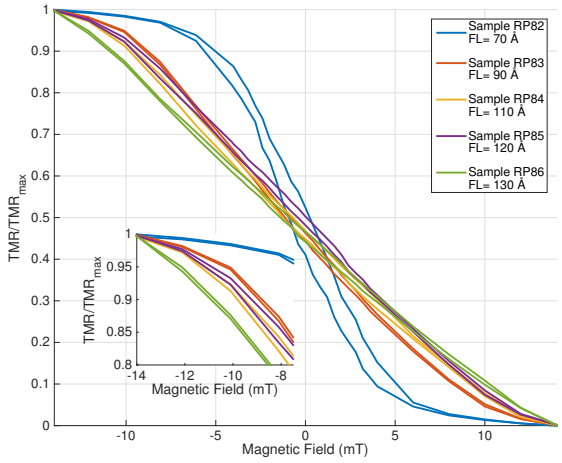


Figure 7: Final optimization of bottom pinned samples with linearization achieved.

### B. Top pinned optimization

The optimization of top pinned MTJs structures followed the same strategy of bottom pinned samples. A VSM measurement was performed to the following stack: Ru 150 Å/IrMn 180 Å/CoFe 30 Å/Ru 6 Å/CoFeB 40 Å/AlOx 2×(7 Å+ 20 seconds of oxidation)/CoFeB 120 Å/Ru 200 Å/Mg 3 Å/Ru 200 Å/Mg 3 Å/Ru 200 Å, with the result being presented in figure 8.

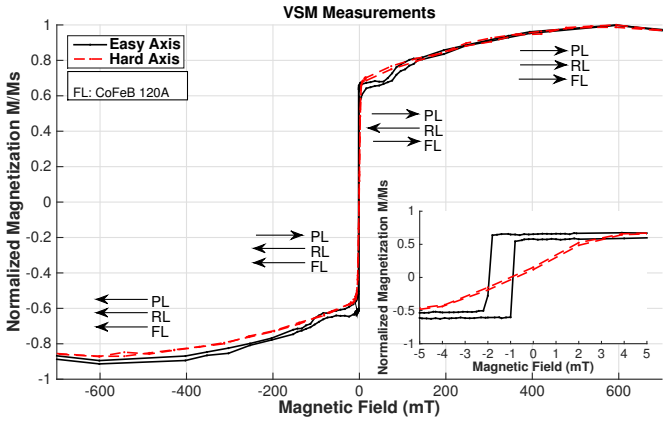


Figure 8: VSM results of top pinned samples with a free layer o 120 Å.

When compared with the results of bottom-pinned samples, there is a decrease of both the field at which the reference layer inverts its magnetization to 48 mT, as also the pinned layer to 74 mT. From the inset, it can be noticed that although this structure presents less coercivity, it is shifted for the left side. These results are re-

lated with different roughness of these layers when compared to the bottom pinned case. Two test samples were processed, with the stack: Ru 150 Å/IrMn 180 Å/CoFe 22 Å/Ru 9 Å/CoFeB 30 Å/AlOx (9Å+ 20 seconds of oxidation)/CoFeB 30 Å/Ru 200 Å/Mg 3 Å/Ru 200 Å/Mg 3 Å/Ru 200 Å. The results are presented on figure 9. The sample RP31 has the stack presented just before, while the sample RP32 has a *Ru* layer with 8 Å instead of 9 Å.

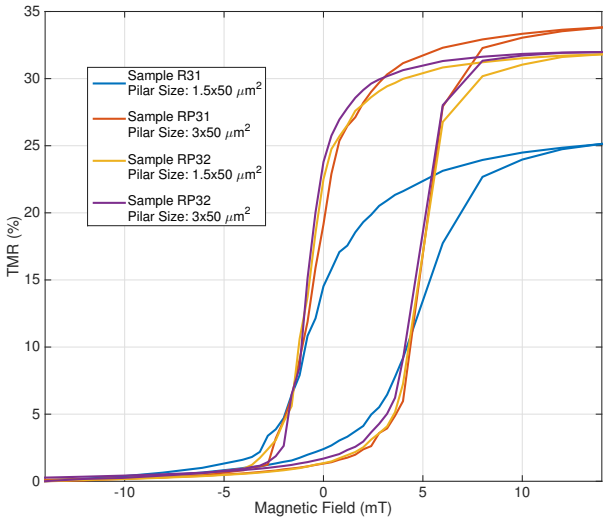


Figure 9: Results of samples with a free layer of 120 Å.

A resume of the results is presented in table V.

Table V: Results of top pinned samples RP31 and RP32.

| Sample ID | Pilar Size ($\mu m^2$) | TMR (%) | R×A ($\Omega.\mu m^2$) | $H_c$ ($mT$) | $H_f$ ($mT$) |
|---|---|---|---|---|---|
| RP31 | 1.5x50 | 25.17 | 8.86 | 2.56 | 2.23 |
| | 3x50 | 33.83 | 4.23 | 2.63 | 2.36 |
| RP32 | 1.5x50 | 31.81 | 3.84 | 2.75 | 2.13 |
| | 3x50 | 31.99 | 1.96 | 2.72 | 1.99 |

As for bottom pinned samples, different barriers were optimized, as well as the thickness of the free layer, with the final result on figure 10.

In order to tune the sensitivity of the sensors, a soft magnet was incorporated on the free layer, *NiFe*. With this layer, sensors with linear responses were obtained, although losing TMR when compared with the previous top pinned sensors with only *(CoFe)B* in the free layer, figure 11.

These samples were deposited in two different machines, due to availability of targets on each one. All

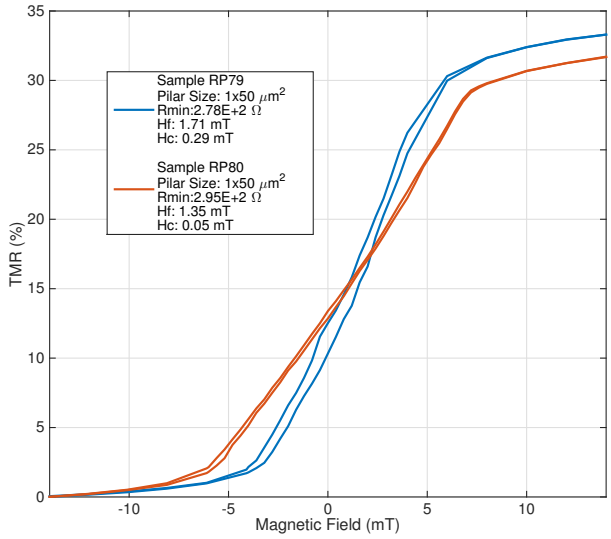


Figure 10: Top pinned samples RP79 and RP80, with linear responses.

Table VI: Free layer optimization with NiFe. The values indicated with * correspond to the deposited value, not to the real value after the complete deposition since there is an etch process in between.

| | | Sample ID | | | | | | |
|---|---|---|---|---|---|---|---|---|
| | | RP125 | RP126 | RP127 | RP128 | RP129 | RP130 | RP131 |
| Layer Composition & Layer Thickness (Å) | Ru | 150 | 150 | 150 | 150 | 150 | 150 | 150 |
| | IrMn | 180 | 180 | 180 | 180 | 180 | 180 | 180 |
| | CoFe | 30 | 30 | 30 | 30 | 30 | 30 | 30 |
| | Ru | 6 | 6 | 6 | 6 | 6 | 6 | 6 |
| | CoFeB | 40 | 40 | 40 | 40 | 40 | 40 | 40 |
| | AlOx | **2×(7Å + 15s)** | | | | | | |
| | **CoFeB** | **20** | **30** | **30** | **30** | **30** | **30** | **40** |
| | **NiFe** | **40*** | **40*** | **60*** | **80*** | **100*** | **120*** | **120*** |
| | Ru | 150 | 150 | 150 | 150 | 150 | 150 | 150 |
| | Ta | 50 | 50 | 50 | 50 | 50 | 50 | 50 |
| | Ru | 150 | 150 | 150 | 150 | 150 | 150 | 150 |
| | Ta | 50 | 50 | 50 | 50 | 50 | 50 | 50 |

layers until *NiFe* were deposited on Nordiko 3600, and the remaining layers were deposited on Nordiko 3000, both machines are similar.

In the first deposition, a 50 Å layer of tantalum was deposited, to protect the *NiFe* layer of oxidation. The samples were then exposed to a soft etch on Nordiko 3000 to remove the *Ta* layer.

The deposition of this barrier, as well as for bottom pinned samples, occurs in two individual steps. First a 7 Å layer of *Al* is deposited and oxidized, and then this process is repeated to create the second layer. The results are presented in figure 11 and resume in table VII.

From the results presented, it is possible to conclude that sample RP125 and RP126 did not achieve a good coupling between the *(CoFe)B* layer and the *NiFe* layer,

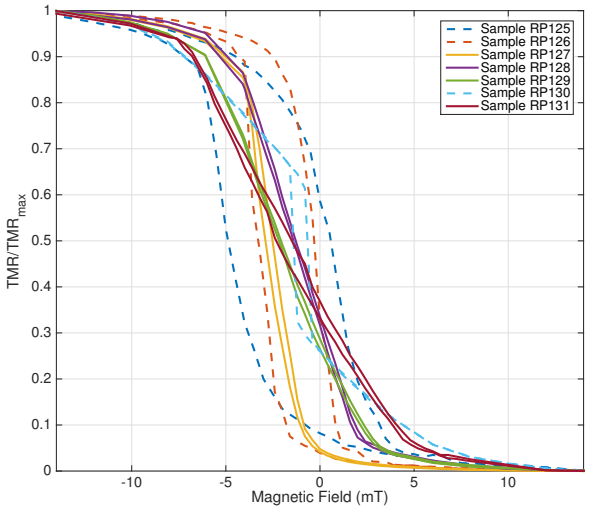


Figure 11: Results of incorporation of *NiFe* on the free layer.

Table VII: Resume of the results for free layer optimization with NiFe.

| Sample | TMR (%) | $H_c$ (mT) | $H_f$ (mT) | $R_{min}$ ($\Omega$) |
|---|---|---|---|---|
| RP125 | 24.62 | 2.72 | 2.15 | 224 |
| RP126 | 28.43 | 1.45 | 1.79 | 1760 |
| RP127 | 28.40 | 0.18 | 2.70 | 527 |
| RP128 | 8.40 | 0.06 | 1.34 | 67 |
| RP129 | 19.39 | 0.05 | 2.12 | 340 |
| RP130 | 16.28 | 0.37 | 1.03 | 396 |
| RP131 | 25.18 | 0.41 | 1.90 | 339 |

since the magnetic response is similar to the response achieved for sensors with only *(CoFe)B* thinner free layers. Sample RP130 also shows a non-linear behavior, probably due to the etch conditions. The remaining samples achieved a linear response as desired.

### C. Study of redeposition in top pinned samples

During the optimization process for top pinned samples, problems related with redeposition of material were detected. This effect consists in material that gets attached to the pillar's side, which will give raise to a low resistance sensor, since the material deposited in the sides will work as conducting channels in parallel with the MTJ pillar.

The redeposition effect is more accentuated in top pinned MTJs, due to the fact that the second etch is longer when compared with bottom pinned samples, and so more material will be projected. To solve this problem, a strategy consisting in cleaning the sides of the pillar during 500 seconds at an angle of 25 ° was adopted, instead of the usual process using an angle of 70 ° until the barrier, and then 40 ° during 200 seconds. The advantage of this strategy is presented in figure 12.

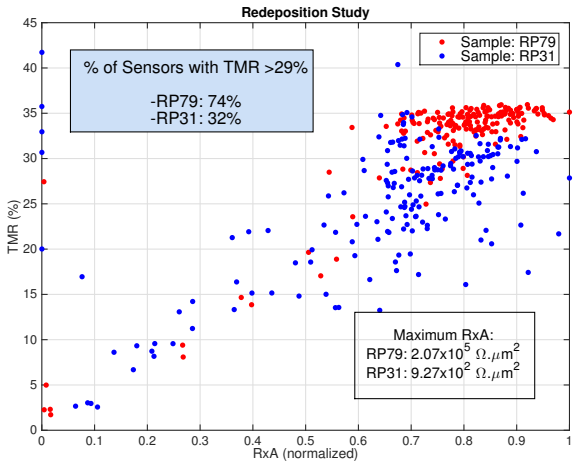


Figure 12: TMR as function of *RA* product. Study of redeposition for two samples.

The result of the sample RP31 is characteristic of redepositon, with lower value of TMR followed by a decrease in resistance. With this new strategy, the yield of working sensors, with TMR larger than 29%, was improved from 32% to 74%.

## IV. CHARACTERIZATION OF THE SENSORS

### A. IV curves

The sensor's response to the increase of current is, in general, dependent of the barrier characteristics. This measurements were performed on sensors with the stack of sample RP129, indicated on table VI.

The decrease of TMR with the applied current can be seen on figure 13. A value of 0.37 V was found as the point for which the TMR is reduced to half of its maximum value.

The breakdown voltage for these type of barrier was found to be 1.3 V.

### B. Noise Characterization

By last, a noise characterization was performed to this type barrier. In order to study the noise response, sensors with and without *NiFe* in the free layer were measured. The results were the same for both free layers, as well as for sensors that were subjected to an annealing treatment. The *RA* product increased after

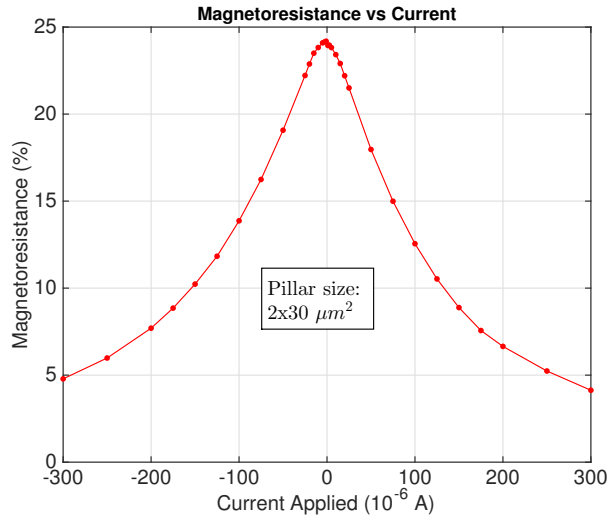


Figure 13: TMR dependence of the applied bias current. Sensor's $R \times A = 210.2\ \ k\Omega.\mu m^2$.

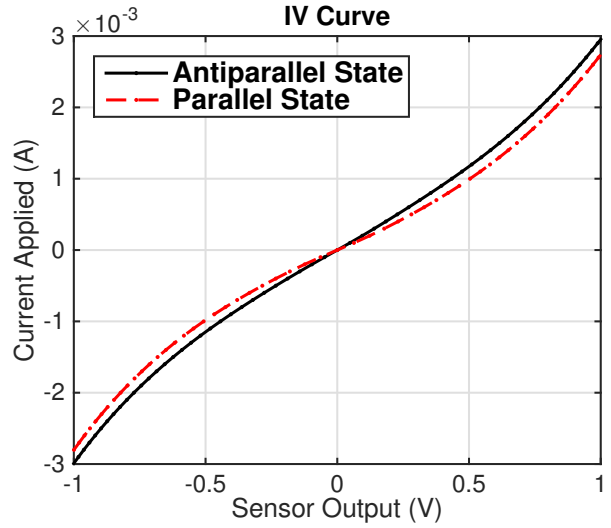


Figure 14: IV curve for an MTJ sensor in parallel and anti-parallel states. Sensor's $R \times A = 210.2\ \ k\Omega.\mu m^2$.

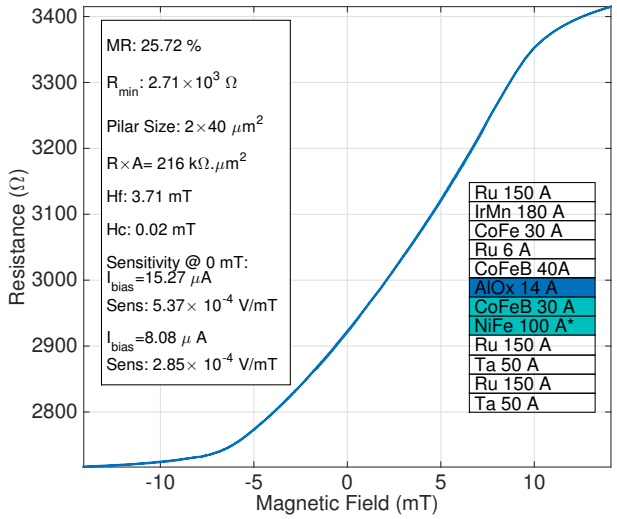


Figure 15: Magnetoresistance response of the sensor, after annealing.

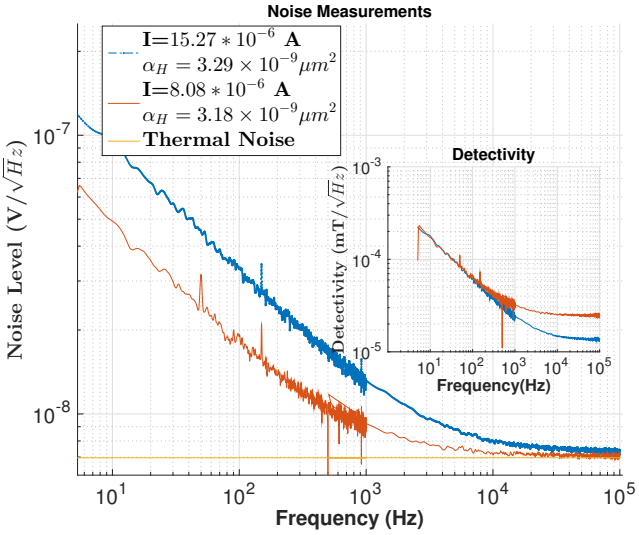


Figure 16: Noise spectral density and detectivity of the sensor after annealing.

annealing, for both stacks. As example, a sensor with $R \times A = 216\ k\Omega.\mu m^2$ before annealing, increased this product to $472\ k\Omega.\mu m^2$ after annealing. The noise measurement corresponding to this sensor after annealing is presented in figure 16. The magnetoresistance response is also presented in figure 15.

Another general result for all sensors, was the loss of sensitivity after annealing, explained by the fact that the free-layer used is too thick, leading to domains that rotate at different fields, as could be seen in some sensors with a non-linear response before annealing. This thermal treatment allows the rearrangement of the atoms and magnetic domains, with a final layer more uniform than before.

The result obtained for the sensor presented before, is a detectivity of 105 $nT/\sqrt{Hz}$ at 30 Hz, and 14 $nT/\sqrt{Hz}$ at 10 kHz, with the noise spectral density characterized by an Hooge parameter of $3.29 \times 10^{-9} \mu m^2$, which meets the results obtained before at INESC-MN and are presented in the literature.

## V. MAGNETOMETER

## VI. FINAL DEVICE

The final device was assembled with four sensors in bridge configuration. The corresponding stack is: Ru 150 Å/IrMn 180 Å/CoFe 30 Å/Ru 6 Å/CoFeB 40 Å/AlOx 14 Å/CoFeB 115 Å/Ru 200 Å/Mg 3 Å/Ru 200 Å/Mg 3 Å/Ru 200 Å. The barrier of these sensors is again deposited in two steps, as explained before. The TMR of the four sensors is 28%, after annealing treatment.

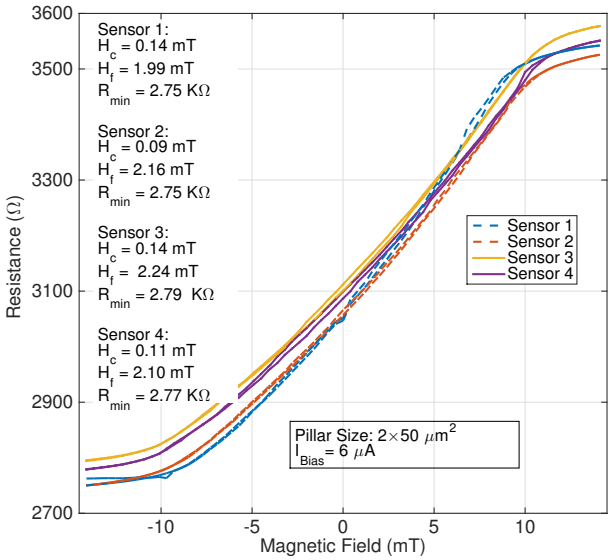


Figure 17: Magnetoresistance response of the sensors, after annealing.

To achieve a bridge response, the sensors need to be assembled with different directions, as presented in figure 4, with sensors indicated as S1 and S2 changing their resistance in the opposite way of sensors S3 and S4. The sensors were connected to a PCB through a wire bonding process, that connects two of the four pads of the sensor to the external device. The PCB used is presented in figure 18(a). This PCB has four connections, with V+ and V- being the output of the bridge, and OUT+ and OUT- the input. It was fabricated to INESC-MN, being present in previous projects as a test device. The final device of this thesis is mainly limited by the dimensions of this structure.

One bridge was placed perpendicular to the other two, measuring fields in the vertical direction. The other two sensors are placed with a difference of 90° in the same plane, measuring the X and Y directions, as presented in figure 18(b). Once connected, the device has two inputs of current, with all bridges being supplied with the same value since they are arranged in series, and 6 outputs corresponding to each of V+ and V- of the 3 bridges.

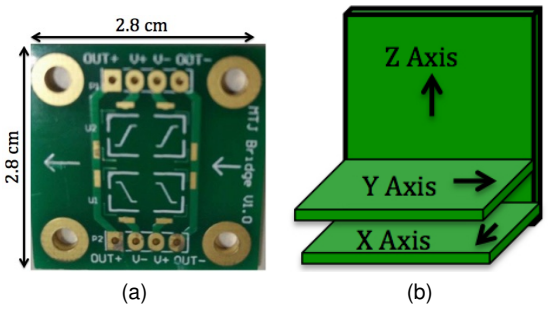


Figure 18: PCB used to achieve a bridge response and schematic of bridges position to measure the three directions of space.

The bridge was tested for different applied currents, with the maximum variation of output for 0.4 mA. For this current bias, a sensitivity of 5.6 mV/mT was achieved between ±10 mT, with and offset value of -6.3 mV. The power consumption is 2.02 mW for the biased current.

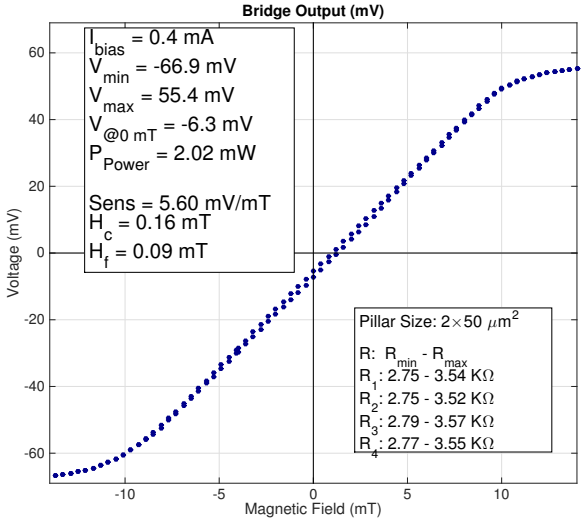


Figure 19: Magnetoresistance response of the complete bridge.

In order to test the device, the magnetic field of a permanent magnet was measured. The sensor was placed in the center of a circumference with a radius of 5 cm, with the magnet changing its position along the circumference, as presented in figure 20. At this distance, the field created by the permanent magnet will never cause the saturation of the sensors, ensuring that the measurement is performed in their linear range.

The result for one axis is presented in figure 21. The offset correction is determinant to obtain coherent values of field, since it should change between the module of a value.

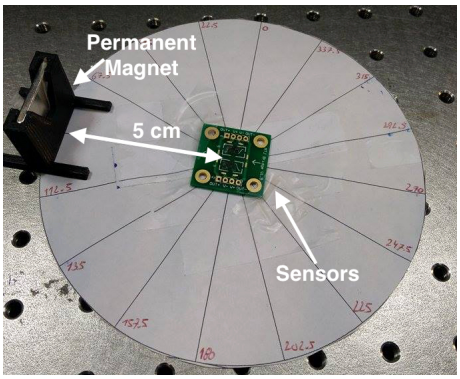


Figure 20: Single bridge being tested.

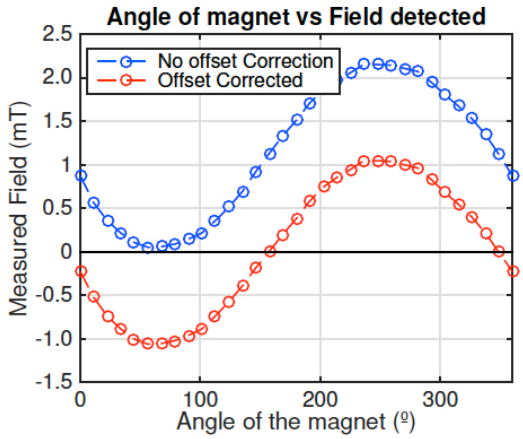


Figure 21: One axis measure of the field from a permanent magnet, with a bias current of 0.4 mA.

When measured in both axis, it is expected a constant module for the field detected, after all, the magnetic field of the magnet is always the same in every position.

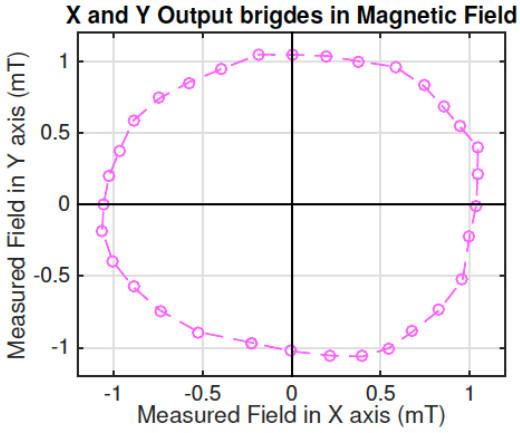


Figure 22: Two axis measure of the field from a permanent magnet, with a bias current of 0.4 mA.

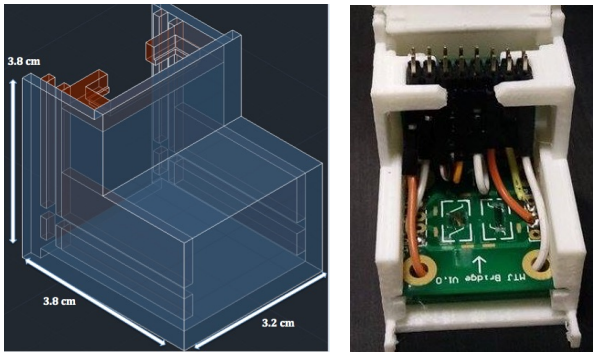


(a) (b)

Figure 23: Shematic and front view of the final device. Dimensions: 3.2x3.8x3.8cm.

The detected magnetic field from the magnet was 1.05 mT with an error of 0.04 mT.

## VII. CONCLUSION

This thesis aimed the development of a 3D-magnetometer capable of measuring magnetic fields in the 3 dimensions of space. This device was based on magnetoresistive sensors, more precisely on magnetic tunnel junctions, using technologies and materials available at INESC-MN research lines.

The MTJs followed a rigorous fabrication process, including stack deposition by ion beam sputtering with a barrier of *AlOx*, oxidized by the *Remote Plasma* method, having the goal to produce a device with a linear response. A barrier of *AlOx* was used instead of MgO, which has higher values of TMR but always requires annealing.

Based on [Ru/IrMn/CoFe/Ru/CoFeB/AlOx/CoFeB/Ru/Ta/Ru/Ta] stacks, with 14 Å Al thick layer, both bottom pinned and top pinned magnetic configurations were optimized, with the second configuration having the advantage of not requiring annealing. For devices with $1\times50$ $\mu m^2$ areas, shape anisotropy was effective in promoting a linear response in bottom pinned samples, with *(CoFe)B* free layer and thickness between 90-120 Å, achieving TMR values of 29%, for R×A of 60 $k\Omega.\mu m^2$. Increasing the free layer to 110 - 120 Å in top pinned configurations, linearization was only possible for dimensions lower or equal to $1 \times 50$ $\mu m^2$, where a TMR of 35% was reached. However, after annealing, sensors with widths of 2 $\mu m^2$ also achieved linearity. In order to reduce the net magnetization of the free layer, which affects the self-demagnetizing field, and allows to tune the sensitivity of the sensor, *NiFe* was incorporated in the free layer, resulting in a decrease in TMR to 29%, but allowing linearization of sensors with dimensions up to $2 \times 50$ $\mu m^2$ even before annealing.

The oxidation time of the barrier was also optimized

for 5 Å and 7 Å thick *Al* films, aiming the deposition of thicker barriers up to 14 Å using a two-step deposition/oxidation method. For barriers of 14 Å, the sensor reduced is TMR for half of the initial value at 0.37 V, a value usually between 0.3-0.5 V, according with the literature.

In addition, noise measurements were performed in top pinned configurations, before and after annealing. The detectivity value is 120 $nT/\sqrt{Hz}$ at 30 Hz and 20 nT$/\sqrt{Hz}$ at 10 KHz, for a linear range between $\pm$10 mT. The annealing increased the R$\times$A of the sensors, leading to a direct increase of the noise density level. However, the Hooge parameter, that was also characterized, with an average result of $4 \times 10^{-9}$ $\mu m^2$, remains constant before and after annealing as demonstrated by the results and according with the literature.

In order to achieve higher yields of working sensors per sample, the processing method was improved to reduce the redeposition of material on pillar's sides, focusing on the second etch conditions, with the second etch angle of 40 $^\circ$ being reduced to 25 $^\circ$, demonstrating an upgrade from 32$\%$ to $74\%$ of operational sensors showing TMR larger than 29$\%$, for top pinned samples.

The final device resulted in a magnetometer assembled with 4 sensors in bridge configuration for each direction (x,y,z), with TMR of $28\%$ and R$\times$A of 270 k$\Omega.\mu m^2$. The bridge was tested under different applied currents, showing a maximum output for 0.4 mA, corresponding to a variation of 122 mV between $\pm$14 mT and a sensitivity of 5.6 mV/mT between $\pm$10 mT. The device was tested and successfully measured the field of a permanent magnet of 1.06 mT, with an error of 0.04 mT.

Future work, would require reducing the dimensions of the final device. With optimized top pinned sensors developed in this research, it is now possible to assemble a bridge directly on the processed wafer, without making use of a discrete assembly. If improved sensitivities are needed to detect smaller fields, then the linear range needs to be reduced. The use of a new generation of sensors capable of sensing magnetic fields out of the plane should also be considered, allowing a significant reduction on the device's final dimensions.

[1] M. Julliere, "Tunneling between ferromagnetic-films," *Physics Letters A*, vol. 3, no. 54, pp. 225–226, 1975.

[2] S. Cardoso, *Dual-Stripe GMR and Tunnel Junction Read Heads and Ion Beam Deposition and Oxidation of Tunnel Junctions*. PhD thesis, Universidade Técnica de Lisboa, IST, 2001.